WRFRFT-based Coherent Detection and Parameter Estimation of Radar Moving Target With Unknown Entry/Departure Time

Xiaolong Li*, Zhi Sun, Tianxian Zhang, Wei Yi, Guolong Cui, and
Lingjiang Kong

School of Information and Communication Engineering
University of Electronic Science and Technology of China
Chengdu, Sichuan, P.R. China, 611731
Corresponding author: Xiaolong Li
Email: xiaolongliuestc@gmail.com

Abstract

A moving target may enter a radar coverage area unannounced and leave after an unspecified period, which implies that the target's entry time and departure time are unknown. In the absence of these time information, target detection and parameter estimation (DAPE) will be severely impacted. In this paper, we consider the coherent detection and parameters estimation problem for a radar moving target with unknown entry time and departure time (that is, the time when the target appears-in/leaves the radar detection field is unknown), involving across range cell (ARC) and Doppler spread (DS) effects within the observation period. A new algorithm, known as window Radon Fractional Fourier transform (WRFRFT) is proposed to detect and estimate the target's time parameters (i.e., entry time and departure time) and motion parameters (i.e., range, velocity and acceleration). The observation values of a maneuvering target are first intercepted and extracted by the window function and searching along the motion trajectory. Then these values are fractional Fourier transformed and well accumulated in the WRFRFT domain, where the DAPE of target could be accomplished thereafter. Experiments with simulated and real radar data sets prove its effectiveness.

Keywords:
Radar moving target, unknown entry/depature time, detection and parameter estimation (DAPE), WRFRFT, across range cell.

1. Introduction

Radar is widely used in military and civilian surveillance because of its ability of working at all-time and under all-weather conditions [1, 2, 3, 4, 5, 6]. Generally speaking, target detection, parameter estimation and target imaging are the three most important functions of modern radars [7, 8, 9], where the performance of target detection and parameter estimation will significantly affect the imaging quality for the target [10, 11, 12]. Therefore, how to improve the performances of target detection and parameter estimation have become important topics in radar research [13, 14, 15].

Long-time coherent accumulation is an effective method to improve the performance of radar target detection and parameter estimation (DAPE) [16]. By stacking the echo signals in the same phase level within a certain observation time, the echo's signal-to-noise ratio (SNR) can be improved to the maximum extent with coherent integration processing [17]. However, due to the movement of the target, the phenomenon of across-range cell (ARC) and Doppler spread (DS) [15] will occur within the accumulation time, leading to the failure of the traditional moving target detection (MTD) method. More importantly, in the actual detection scene, the target's time parameters information (that is, when the target enters and leaves the radar detection area) and motion parameters information (i.e., distance, velocity, and acceleration) are often unknown, which will bring great challenges to the DAPE of moving targets with long time coherent integration.

To deal with the ARC and realize the coherent detection of constant velocity targets, many methods have been proposed, such as location rotation transform (LRT) [18], sequence reversing transform (SRT) [19], Radon Fourier transform (RFT) [20, 21, 22], scaled inverse Fourier transform (SIFT) [23] and keystone transform (KT) [24, 25, 26]. More specifically, LRT and RFT eliminate the ARC by two-dimensional searching processing in the parameter space, while SRT and SIFT are able to eliminate the ARC via the correlation operation without the brute-force searching process. Unfortunately, when the moving target has a certain degree of mobility (e.g., with acceleration), the methods in [18, 19, 20, 21, 22, 23, 24, 25, 26] may suffer integration and detection performance loss since they could not remove the ARC and DS caused by target's acceleration motion.

As to the accelerating target, it is worth noting that the ARC (including

the ARC induced by velocity and the ARC caused by acceleration) and DS effects occur simultaneously during the observation time. To jointly correct and compensate for the ARC and DS, Xu, et al. [27] introduced a method known as generalized Radon Fourier transform (GRFT), which is the extension of the original RFT algorithm. In addition, Li, et al. [28] proposed an algorithm named Radon Lv's distribution (RLVD) to accumulate and detect weak target signals, while Chen, et al. [29] proposed the Radon Fractional Fourier transform (RFRFT) for a maneuvering target detection. To some extent, these two algorithms [28, 29] also can be regarded as the expansion and extension of the RFT, since both RLVD and RFRFT eliminate the ARC and DS simultaneously by searching in the range-velocity-acceleration domain. However, the computational complexity of RLVD/RFRFT is bigger than that of GRFT.

Moreover, there are some other coherent integration algorithms, which could be employed to deal with the ARC and/or DS, such as short time GRFT (STGRFT) [30], symmetric autocorrelation function [31], adjacent correction function [32, 33, 34], KT with matched filter process [35], three-dimensional scaled transform [36], and so on. In particular, the STGRFT-based method is able to remove the ARC/DS and obtain the coherent integration. However, the STGRFT-based method only considers the detection problem of a moving target. Most importantly, STGRFT and the other existing algorithms mentioned above [18, 19, 20, 21, 22, 23, 24, 25, 26, 27, 28, 29, 30, 31, 32, 33, 34, 35, 36] are all assume that the target's time parameter information (that is, the time when the target entries/leaves the radar detection area) is already known. Actually, before the target detection and parameters estimation are accomplished, the time of target's entry and leaving is often unknown, and then this assumption will no longer hold and the existed coherent integration methods would become invalid, or at least degraded.

This paper addresses the coherent detection and parameters estimation problem for a radar moving target with unknown entry/departure time, where the ARC and DS effects are also considered. A new method known as window Radon Fractional Fourier transform (WRFRFT) is proposed to estimate the target's time parameters (i.e., entry time and departure time) and motion parameters (i.e., range, velocity and acceleration). By employing the window function and searching process within the parameter space, the WRFRFT is capable to remove the ARC/DS effect and realize the coherently refoucusing of target signal, resulting in superior SNR improvement and bet-

ter detection and parameter estimation ability. Detailed experiments with simulated data and real radar data are given to demonstrate the superiority of the WRFRFT-based method.

The signal model for a radar moving target with unknown entry time and departure time is described in Section 2. In section 3, the proposed WRFRFT method is given, including its definition, properties, main steps and computational complexity. In Section 4, the performances of WRFRFT method with simulated and real data are assessed. Section 5 presents the conclusions.

2. Mathematical Model of Received Signal

Assume that the linear frequency modulation is adopted as the radar's transmitted waveform, i.e.,

$$s_{trans}(\hat{t}) = \text{rect}\left(\frac{\hat{t}}{T_p}\right) \exp\left(j\pi\gamma\hat{t}^2\right) \exp(j2\pi f_c\hat{t}) \tag{1}$$

where $\text{rect}\,(x) = \begin{cases} 1, & |x| \leq 0.5 \\ 0, & |x| > 0.5 \end{cases}$, $\hat{t}$, γ, f_c and T_p denote, respectively, the fast time variable, chirp rate, carrier frequency and pulse duration.

Suppose that the total observation time of radar is from T_0 to T_1, where a moving target enters the radar detection area at time T_b and leaves the radar detection area at time T_e ($T_0 < T_b < T_e < T_1$). The instantaneous slant distance between the target and radar at time T_b is denoted as R_0, and the radial distance of target could be expressed as:

$$R(t) = R_0 + V(t - T_b) + A(t - T_b)^2, t \in [T_b, T_e] \tag{2}$$

where t denotes the slow time, while V and A are respectively the target's radial velocity and acceleration, T_b represents the beginning-time (entry) of the target and T_e represents the ending-time (departure) of the target, which are both unknown.

With the pulse compression (PC), the received signal within the observation time can be expressed as [27]

$$s(\hat{t}, t) = w(t)\sigma_0\text{sinc}\left[B\left(\hat{t} - \frac{2R(t)}{c}\right)\right]$$
$$\times \exp\left[-j4\pi\frac{R(t)}{\lambda}\right] + n_s(\hat{t}, t) \tag{3}$$

4

where

$$w(t) = \text{rect}\left[\frac{t - 0.5(T_b + T_e)}{T_e - T_b}\right] = \begin{cases} 1, & T_b \leq t \leq T_e \\ 0, & \text{else} \end{cases} \tag{4}$$

$n_s(\hat{t}, t)$ represents noise, σ_0 and λ are respectively the signal amplitude and the wavelength, while B and c represent the bandwidth and light speed, respectively.

From (3), it could be noticed that the radar echo contains target signal within the period $[T_b, T_e]$, while the radar echo only contains noise for the other time periods, i.e., the beginning time of target signal is T_b and the ending time of target signal is T_e. The sketch map of the radar echo in the $\hat{t}$-t plane is given in Fig. 1.
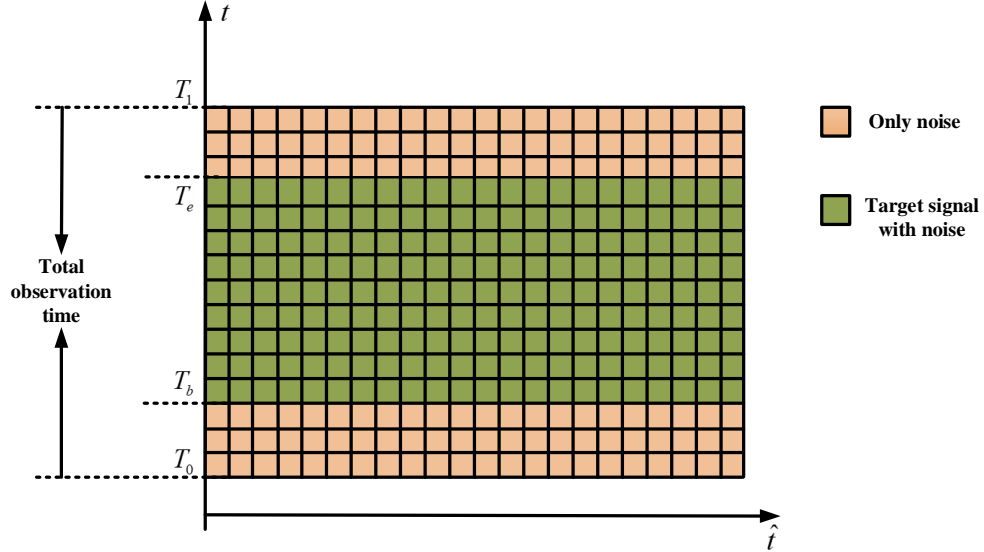
Figure 1: Sketch map of the radar's echo in the $\hat{t}$-t plane.

3. WRFRFT-based Method

3.1. Definition of WRFRFT

The definition of WRFRFT is given as

$$\begin{aligned} WR_{g(t)}(\alpha, u) &= F_\alpha[g(t)s\left(2r(t)/c, t\right)](u) \\ &= \int_{-\infty}^{\infty} g(t)s\left(2r(t)/c, t\right) K_a(t, u)dt, \end{aligned} \tag{5}$$

5

where $g(t)$ and $r(t)$ are respectively the window function and searching motion trajectory:

$$r(t) = r_0 + v(t - \eta_0) + a(t - \eta_0)^2 \tag{6}$$

$$g(t) = \text{rect}\left[\frac{t - 0.5(\eta_1 + \eta_0)}{\eta_1 - \eta_0}\right] = \begin{cases} 1, & \eta_0 \le t \le \eta_1 \\ 0, & \text{else} \end{cases} \tag{7}$$

$$T_0 \le \eta_0 \le \eta_1 \le T_1$$

η_0 is the beginning time of $g(t)$ and η_1 is ending time of $g(t)$, (r_0, v, a) denotes the searching motion parameters pair (i.e., searching initial range, searching radial velocity and radial acceleration). $\alpha = P\pi/2$ is the rotation angle, P is searching transform order, F_α represents the FRFT operator, and the transform kernel $K_a(t, u)$ is given by

$$K_a(t, u) = \begin{cases} A_\alpha \exp[j(0.5t^2 \cot \alpha - ut \csc \alpha + 0.5u^2 \cot \alpha)] & \alpha \ne n\pi \\ \delta[u - (-1)^n t] & \alpha = n\pi \end{cases} \tag{8}$$

where $A_\alpha = \sqrt{(1 - j \cot \alpha)/2\pi}$.

Inserting (7) into (5) yields,

$$WR_{g(t)}(\alpha, u) = \int_{\eta_0}^{\eta_1} g(t) s\left(2r(t)/c, t\right) K_a(t, u) dt \tag{9}$$

From the definition of WRFRFT, it could be interpreted as the transform of the target's intercepted and extracted signal in the FRFT domain. In particular, the WRFRFT includes three main steps: The first is an interception of the two-dimensional compressed signal based on function $g(t)$ (i.e., $g(t)$ determines the interception-operation's beginning/ending time). The second is the signal extraction process applied to the intercepted signal, based on the resultant searching motion parameters pair (r_0, v, a). The third is the FRFT-based integration process.

For comparison, the definition of RFRFT is also given:

$$RFRFT(\alpha, u) = F_\alpha[s\left(2r(t)/c, t\right)](u)$$
$$= \int_{-\infty}^{\infty} s\left(2r(t)/c, t\right) K_a(t, u) dt \tag{10}$$
$$= \int_{T_0}^{T_1} s\left(2r(t)/c, t\right) K_a(t, u) dt$$

6

From (9) and (10), we can notice that both WRFRFT and RFRFT extract the signal along target's motion trajectory and integrate with FRFT. The main difference is that RFRFT performs the extraction and integration operations within the total observation time, while the beginning/ending time of WRFRFT is adjustable (determined by η_0 and η_1), thus able to better match with the moving target with unknown entry/departure time. In particular, the RFRFT can be considered as a special case of WRFRFT (i.e., when $\eta_0 = T_0, \eta_1 = T_1$).

3.2. Some Properties of WRFRFT

1) Rotational Additivity: Note that the kernel of WRFRFT has the rotational additivity property, i.e.,

$$\int_{-\infty}^{\infty} K_\alpha(t, u) K_\beta(u, z) du = K_{\alpha+\beta}(t, z) \tag{11}$$

Thus, it could be easily for us to obtain the rotational additivity of WRFRFT, i.e.,

$$
\begin{aligned}
WR_{g(t)}(&\alpha + \beta, z) \\
&= F_\beta[WR_{g(t)}(\alpha, u)](z) \\
&= \int_{-\infty}^{\infty} K_\beta(u, z) \int_{-\infty}^{\infty} g(t) s\left(2r(t)/c, t\right) K_\alpha(t, u) dt du \\
&= \int_{-\infty}^{\infty} g(t) s\left(2r(t)/c, t\right) \int_{-\infty}^{\infty} K_\alpha(t, u) K_\beta(u, z) du dt \\
&= \int_{-\infty}^{\infty} g(t) s\left(2r(t)/c, t\right) K_{\alpha+\beta}(t, z) dt \\
&= F_{\alpha+\beta}[g(t) s\left(2r(t)/c, t\right)](z)
\end{aligned}
\tag{12}
$$

The rotational additivity of WRFRFT provides us the solution of the transform between WRFRFTs with different transform angles. That is to say, we only need to calculate WRFRFT with the total transform order for one time, which is a major advantage in term of computational efficiency.

2) Inverse WRFRFT (IWRFRFT): According to the rotational additivity property above, it also could be concluded that the WRFRFT of angle $-\alpha$ is the inverse of the WRFRFT with angle α, since that $F_{-\alpha}(F_\alpha) = F_{\alpha-\alpha} = F_0 = I$. The IWFRFT is

$$g(t) s\left(2r(t)/c, t\right) = \int_{-\infty}^{\infty} WR_{g(t)}(\alpha, u) K_{-\alpha}(t, u) du \tag{13}$$

7

3) Linear Additivity: It's easy to find that WRFRFT is linear. In particular, let ε_1 and ε_2 denote two constant coefficients, and we have

$$F_\alpha[\varepsilon_1 x_1 + \varepsilon_1 x_2](u) = \varepsilon_1 F_\alpha[x_1](u) + \varepsilon_1 F_\alpha[x_2](u) \tag{14}$$

This property shows that the WRFRFT satisfies the superposition principle, which is helpful in the analysis of multi-component signals.

4) Index Commutativity: Apply (5) for two orders, we have

$$
\begin{aligned}
&F_\beta[F_\alpha[g(t)s\,(2r(t)/c,t)](z)]\\
&= \int_{-\infty}^{\infty} K_\beta(u,z) \int_{-\infty}^{\infty} g(t)s\,(2r(t)/c,t)\,K_\alpha(t,u)dtdu\\
&= \int_{-\infty}^{\infty} K_\alpha(t,u) \left[\int_{-\infty}^{\infty} g(t)s\,(2r(t)/c,t)\,K_\beta(u,z)du \right] dt\\
&= F_\alpha[F_\beta[g(t)s\,(2r(t)/c,t)](z)]
\end{aligned}
\tag{15}
$$

Hence, the WRFRFT adheres to the index commutativity property.

5) Parseval Relation: The WRFRFT also holds the classical Parseval relation:

$$
\begin{aligned}
&\int_{-\infty}^{\infty} g(t)x\,(2r_x(t)/c,t)\,y\,(2r_y(t)/c,t)\,dt\\
&= \int_{-\infty}^{\infty} WR_x\,(\alpha,u)\,WR_y^*\,(\alpha,u)\,du
\end{aligned}
\tag{16}
$$

where $WR_x\,(\alpha,u) = F_\alpha[g(t)x(t,2r_x(t)/c](u)$, $WR_y\,(\alpha,u) = F_\alpha[g(t)y(t,2r_y(t)/c](u)$. In particular, (16) will turn into the energy conservation property when $x = y$, i.e.,

$$\int_{-\infty}^{\infty} g(t)|x\,(2r_x(t)/c,t)\,|^2 dt = \int_{-\infty}^{\infty} |WR_x\,(\alpha,u)\,|^2 du \tag{17}$$

The squared magnitude of the WFRFT ($|WR_x\,(\alpha,u)\,|^2$) thus represent the signal energy spectrum with angle α and window function $g(t)$.

8

3.3. WRFRFT for Moving Target Detection and Estimation

Substitute (3) and (4) into (5) yields,

$$
\begin{aligned}
WR_{g(t)}(\alpha, u) &= F_\alpha[g(t)s\,(2r(t)/c, t)](u) \\
&= \int_{-\infty}^{\infty} g(t)w(t)\sigma_0 \mathrm{sinc}\left[B\left(\frac{2r(t)}{c} - \frac{2R(t)}{c}\right)\right] \\
&\quad \times \exp\left[-j4\pi\frac{R(t)}{\lambda}\right] K_\alpha(t, u)dt \\
&\quad + \int_{-\infty}^{\infty} g(t)n_s(2r(t)/c, t)K_\alpha(t, u)dt
\end{aligned}
\tag{18}
$$

where the first and the second integral term of (18) represent respectively the WRFRFT of target signal and the WRFRFT of noise.

Let C and D are respectively:

$$
C = \{t|g(t) = 1\}, D = \{t|w(t) = 1\}
\tag{19}
$$

In other words, C denotes the function $g(t)$'s non-zero area while D denotes the function $w(t)$'s non-zero area.

Case 1: When $C \cap D = \varnothing$, we have

$$
g(t)w(t) = 0
\tag{20}
$$

In this case, (18) could be expressed as

$$
\begin{aligned}
WR_{g(t)}(\alpha, u) &= 0 + \int_{-\infty}^{\infty} g(t)n_s(2r(t)/c, t)K_\alpha(t, u)dt \\
&= \int_{\eta_0}^{\eta_1} n_s(2r(t)/c, t)K_\alpha(t, u)dt
\end{aligned}
\tag{21}
$$

Hence, in this case, only noise is extracted and accumulated, but none of the target's signal is extracted and accumulated.

Case 2: When $C \cap D \neq \varnothing$, we have

$$
g(t)w(t) = \begin{cases} 1, & T' \leq t \leq T'' \\ 0, & \text{else} \end{cases}
\tag{22}
$$

where

$$
T' = \max[T_b, \eta_0], T'' = \min[T_e, \eta_1]
\tag{23}
$$

In this case, the WRFRFT of (18) can be recast as

$$
\begin{aligned}
WR_{g(t)}(\alpha, u) = & \int_{T'}^{T''} \sigma_0 \text{sinc}\left[B\left(\frac{2r(t)}{c} - \frac{2R(t)}{c}\right)\right] \\
& \times \exp\left[-j4\pi\frac{R(t)}{\lambda}\right] K_\alpha(t, u)dt \\
& + \int_{\eta_0}^{\eta_1} n_s(2r(t)/c, t)K_\alpha(t, u)dt
\end{aligned}
\tag{24}
$$

From (23) and (24), we notice that the values of η_0 and η_1 determine the extracted range of the target signal and noise. In order to ensure SNR improvement, on the one hand, we need to extract and integrate all the target signals, and at the same time, we need to extract as little noise as possible.

In particular, to guarantee that all the target signals are extracted and accumulated, the following equation should be satisfied

$$
T' \leq T_b, T'' \geq T_e
\tag{25}
$$

Combining with (23) we have

$$
\eta_0 \leq T_b, \eta_1 \geq T_e
\tag{26}
$$

In addition to satisfying the inequality (26), we also need to ensure that as little noise as possible is extracted. Thus, we have

$$
\eta_0 = T_b, \eta_1 = T_e
\tag{27}
$$

Then (24) could be rewritten as:

$$
\begin{aligned}
WR_{g(t)}(\alpha, u) = & \int_{T_b}^{T_e} \sigma_0 \text{sinc}\left[B\left(\frac{2r(t)}{c} - \frac{2R(t)}{c}\right)\right] \\
& \times \exp\left[-j4\pi\frac{R(t)}{\lambda}\right] K_\alpha(t, u)dt \\
& + \int_{T_b}^{T_e} n_s(2r(t)/c, t)K_\alpha(t, u)dt \\
= & \int_{T_b}^{T_e} \sigma_0 \exp\left[-j4\pi\frac{R(t)}{\lambda}\right] K_\alpha(t, u)dt \\
& + \int_{T_b}^{T_e} n_s(2r(t)/c, t)K_\alpha(t, u)dt \\
& \text{when } r_0 = R_0, v = V, a = A
\end{aligned}
\tag{28}
$$

10

Equation (28) shows that the entire target signal is extracted and could be coherently integrated in the FRFT domain when the motion parameters of the search match with the motion parameters of target.

Based on the analysis above, it could be noticed that only when $\eta_0 = T_b, \eta_1 = T_e$, the target signal is totally extracted and accumulated in the FRFT domain while it could ensure that as little noise as possible is extracted simultaneously, resulting in a peak value in the WRFRFT output (where the peak location corresponds to the time parameters and motion parameters of target).

With different searching parameters (i.e., beginning/ending time, range, velocity and acceleration), different integration outputs of WRFRFT would be obtained and the target signal will be focused as a peak when the searching time/motion parameters match with the target's time/motion parameters. Thus, the target's time parameters and motion parameters could be estimated by

$$(\hat{T}_b, \hat{T}_e, \hat{R}_0, \hat{V}, \hat{A}) = \underset{(\eta_0, \eta_1, r_0, v, a)}{\arg \max} \; |WR_{g(t)}(\alpha, u)| \tag{29}$$

A simulation experiment (Table 1 shows the radar parameters and Table 2 gives the target parameters) is given to show how the WRFRFT performs with varying η_0 and η_1. The result of the radar echo after pulse compression is shown in Fig. 2(a). The WRFRFT result when $\eta_0 = 0.755s$ and $\eta_1 = 3s$ (i.e., the WRFRFT's window function matches the beginning/ending time of target signal) is given in Fig. 2(b) (slice of velocity and acceleration). It is observed that the target signal is coherently accumulated as a peak, which is corresponding to the target's radial velocity and acceleration. Fig. 2(c) and Fig. 2(d) give respectively the WRFRFT results for the cases that $\eta_0 = 0.15s, \eta_1 = 0.5s$ and $\eta_0 = 3.05s, \eta_1 = 3.5s$. In these two cases (Fig. 2(c) and Fig. 2(d)), only noise is extracted and accumulated, resulting in unfocused results for WRFRFT. Fig. 2(e) gives the WRFRFT output when $\eta_0 = 0.505s$ and $\eta_1 = 2.9s$, where only part of the target signal is extracted in this case, and thus the peak value of Fig. 2(e) is smaller than the peak value of Fig. 2(b). Fig. 2(f) shows the WRFRFT output when $\eta_0 = 0.755s, \eta_1 = 3.4s$, where the entire target signal is extracted and coherently accumulated in this case. However, it is worth pointing out that compared with Fig. 2(b), much more noise is extracted and accumulated in Fig. 2(f). As a result, the peak value of Fig. 2(f) is smaller than the peak value of Fig. 2(b).

In Fig. 2(g), we examine the WRFRFT outputs for a fixed η_1 ($\eta_1 = 3$)

but varying η_0. In other words, with the ending time of WRFRFT' window function $g(t)$ matches the target signal's ending time, the peak value reaches its maximum value when $\eta_0 = 0.755s$ (i.e., the beginning time of $g(t)$ equals to the target signal's beginning time). Similarly, Fig. 2(h) shows the integrated peak value of WRFRFT for a fixed η_0 ($\eta_0 = 0.755s$) but varying η_1. That is to say, the beginning time of $g(t)$ matches the target signal's beginning time. We could see that the peak value reaches its maximum value when $\eta_1 = 3s$ (i.e., the ending time of $g(t)$ equals to the target signal's ending time).

Based on the results of Fig. 2, it can be assured that only when the beginning/ending time of WRFRFT's window function equal to the target signal's beginning/ending time, then the integrated output of WRFRFT will reach its maximum value.

Table 1

Radar Parameters

Carrier frequency	6 GHz
Bandwidth	10 MHz
Sample frequency	50 MHz
Pulse repetition frequency	200 Hz
Pulse duration	10 us
Beginning time of target	0.755s
SNR after PC	4 dB

Table 2

Moving Target's Time Parameters and Motion Parameters

Initial range cell	287
Radial velocity (m/s)	90
Radial acceleration (m/s^2)	26
Beginning time	0.755s
Ending time	3s

3.4. Procedure of the WRFRFT-based Method
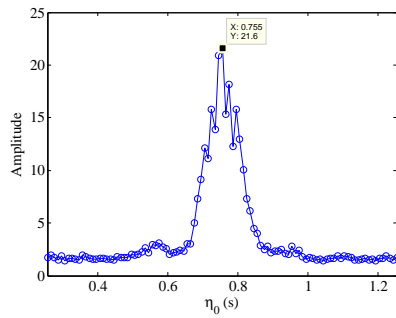
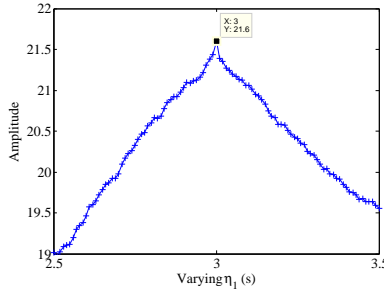The main steps of the WRFRFT-based approach can be summarized as follows:

13
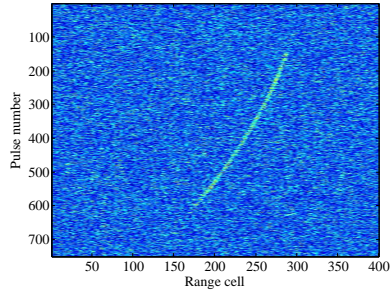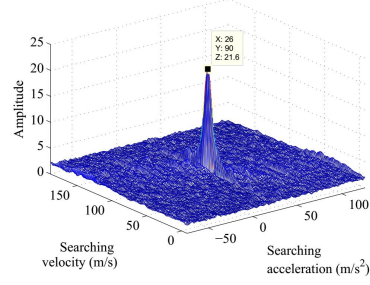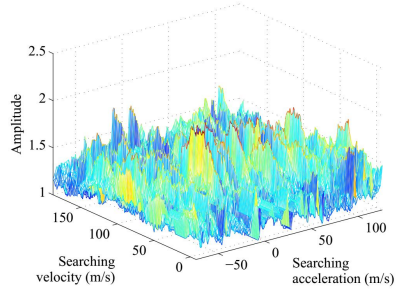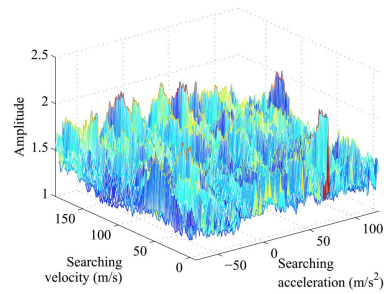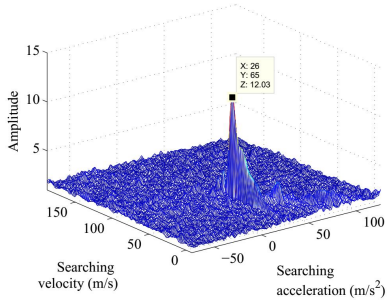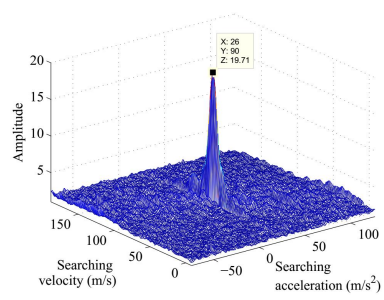
Figure 2: WRFRFT response with respect to η_0 and η_1. (a) PC. (b) $\eta_0 = 0.755s, \eta_1 = 3s$. (c) $\eta_0 = 0.15s, \eta_1 = 0.5s$. (d) $\eta_0 = 3.05s, \eta_1 = 3.5s$. (e) $\eta_0 = 0.505s, \eta_1 = 2.9s$. (f) $\eta_0 = 0.755s, \eta_1 = 3.4s$. (g) Integrated peak value curve for fixed η_1 but varying η_0. (h) Integrated peak value curve for fixed η_0 but varying η_1.

Step 1: Based on the relative prior information of targets to be expected (such as moving status and varieties) and the radar parameters, the searching scope of initial range, velocity, acceleration and beginning/ending time can be obtained (denoted respectively as $[r_{\min}, r_{\max}]$, $[v_{\min}, v_{\max}]$, $[a_{\min}, a_{\max}]$, $[\eta_{0\min}, \eta_{0\max}]$ and $[\eta_{1\min}, \eta_{1\max}]$). In addition, the searching interval of beginning/ending time, initial range, velocity and acceleration can be set as [29]:

$$\Delta\eta = PRT \tag{30}$$

$$\Delta r = c/2B \tag{31}$$

$$\Delta v = \lambda/2(T_1 - T_0) \tag{32}$$

$$\Delta a = \lambda/2(T_1 - T_0)^2 \tag{33}$$

where PRT is radar pulse repetition time.

Step 2: With the searching parameters $(r_s, v_s, a_s, \eta_{0s}, \eta_{1s})$, the moving trajectory to be searched and the window function $g(t)$ could be respectively expressed as:

$$r_s(t) = r_{0s} + v_s(t - \eta_{0s}) + a_s(t - \eta_{0s})^2, t \in [\eta_{0s}, \eta_{1s}] \tag{34}$$

$$g(t) = \text{rect}\left[\frac{t - 0.5(\eta_{1s} + \eta_{0s})}{\eta_{1s} - \eta_{0s}}\right] \tag{35}$$

where $r_{0s} = r_{\min} : \Delta r : r_{\max}$, $v_s = v_{\min} : \Delta v : v_{\max}$, $a_s = a_{\min} : \Delta a : a_{\max}$, $\eta_{0s} = \eta_{0\min} : \Delta\eta : \eta_{0\max}$, $\eta_{1s} = \eta_{1\min} : \Delta\eta : \eta_{1\max}$.

Step 3: Intercept and extract the target signal from the compressed signal based on the window function and searching motion trajectory, i.e.,

$$s_e(t) = g(t)s(2r_s(t)/c, t) \tag{36}$$

Step 4: Apply the WRFRFT operation on the extracted signal.

Step 5: Go through all the searching parameters and obtain the corresponding WRFRFT output $WR_{g(t)}(\alpha, u)$.

Step 6: Take the amplitude of WRFRFT output in step 5 as test statistic, and compare with the adaptive threshold for a given false alarm probability

$$|WR_{g(t)}(\alpha, u)| \underset{H_0}{\overset{H_1}{\gtrless}} \gamma \tag{37}$$

14

where γ dentoes the detection threshold [29], which could be obtained via the reference unit after WRFRFT. If $|WR_{g(t)}(\alpha, u)|$ is larger than γ, target is confirmed. In addition, the target's time parameters and motion parameters can be estimated via the peak location of $WR_{g(t)}(\alpha, u)$.

Fig. 3 gives the flow chart of the WRFRFT-based method.

3.5. Discussion on Computational Complexity

It could be noticed that the WRFRFT mainly involves the five dimensions searching (i.e., searching of beginning time, ending time, range, velocity and acceleration) and the FRFT operation. Note that the coherent integration of the target signal is obtained when the searching time/motion parameters match with the target's time/motion parameters and the fractional order of FRFT matches the target's acceleration. Therefore, the following relationship could be employed within the WRFRFT:

$$\alpha = \text{arccot}\left(\frac{-2a_s T_\eta}{\lambda f_s}\right) \tag{38}$$

where $T_\eta = \eta_{1s} - \eta_{0s} + PRT$ and f_s denotes the sample frequency.

According to the analysis in Section 3.4, the searching numbers of beginning time, ending time, range, velocity and acceleration are:

$$N_{\eta_0} = \text{round}\left(\frac{\eta_{0\max} - \eta_{0\min}}{\Delta\eta}\right) \tag{39}$$

$$N_{\eta_1} = \text{round}\left(\frac{\eta_{1\max} - \eta_{1\min}}{\Delta\eta}\right) \tag{40}$$

$$N_r = \text{round}\left(\frac{r_{\max} - r_{\min}}{\Delta r}\right) \tag{41}$$

$$N_v = \text{round}\left(\frac{v_{\max} - v_{\min}}{\Delta v}\right) \tag{42}$$

$$N_a = \text{round}\left(\frac{a_{\max} - a_{\min}}{\Delta a}\right) \tag{43}$$

Then, the computational complexity of the WRFRFT-based approach is $O(N_{\eta_0} N_{\eta_1} N_r N_v N_a N \log_2 N)$, where N is the pulse number. The computational cost of RFRFT is in the order of $O(N_r N_v N_a N_P N \log_2 N)$ [29], where N_P denotes the number of transform order of FRFT. Hence, the computational burden of WRFRFT is bigger than that of RFRFT, since the searching process of beginning/ending time. It is necessary to study the fast implementation of WRFRFT method in the future.
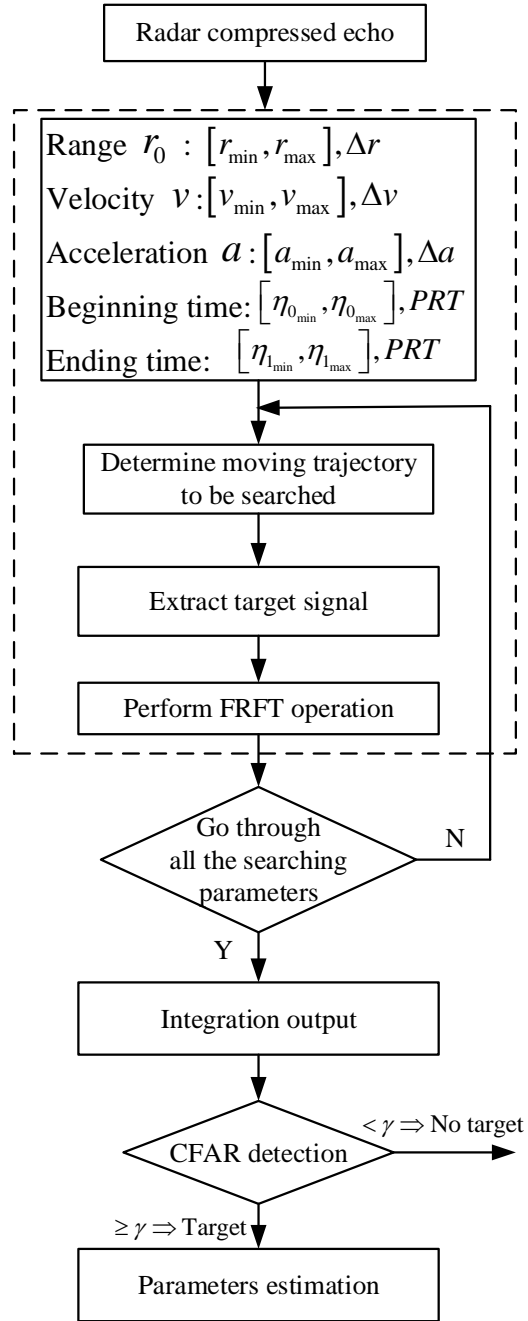
Radar compressed echo

Range r_0 : $\left[r_{\min},r_{\max}\right],\Delta r$

Velocity v : $\left[v_{\min},v_{\max}\right],\Delta v$

Acceleration a : $\left[a_{\min},a_{\max}\right],\Delta a$

Beginning time: $\left[\eta_{0_{\min}},\eta_{0_{\max}}\right],PRT$

Ending time: $\left[\eta_{1_{\min}},\eta_{1_{\max}}\right],PRT$

Determine moving trajectory to be searched

Extract target signal

Perform FRFT operation

Go through all the searching parameters

N

Y

Integration output

CFAR detection

$<\gamma \Rightarrow$ No target

$\geq \gamma \Rightarrow$ Target

Parameters estimation

Figure 3: Flowchart of the WRFRFT method.

16

4. Experiments and Analysis

The experiments with simulated data (Section 4.1, Section 4.2, Section 4.3 and Section 4.4) and real data (Section 4.5) are given to demonstrate the effectiveness of the WRFRFT method, where the radar parameters of Section 4.1, Section 4.2, Section 4.3 and Section 4.4 are set as the same as those in Table 1. In addition, the target's time parameters and motion parameters of Section 4.1−Section 4.2 are given in Table 2. Several typical coherent detection algorithms (RFRFT, GRFT, RFT) are used for comparison.

4.1. WRFRFT of Weak Target

In Fig. 4, the WRFRFT's response for a weak target is given, where the SNR after PC is 0 dB (as shown in Fig. 4(a)). Fig. 4(b)−Fig. 4(f) give respectively different projections of the WRFRFT output. More specifically, the projection in range cell-velocity domain is shown in Fig. 4(b) and the projection in range cell-acceleration domain is given in Fig. 4(c). Meanwhile, the projection in velocity-acceleration space is shown in Fig. 4(d) and the projection in acceleration-beginning time domain is given in Fig. 4(e). It can be noticed that the peak locations of different projections (e.g., Fig. 4(b), Fig. 4(c), Fig. 4(d)) indicate the corresponding parameters (e.g., range, velocity, acceleration, beginning time) of target. Also, the projection in beginning time-ending time space is shown in Fig. 4(f), where Fig. 4(g) and Fig. 4(h) give respectively the beginning time response slice and the ending time response slice of Fig. 4(f), from which we could obtain the estimations of the beginning/ending time of target signal.

In order to comparison, the processing results of RFRFT, GRFT and RFT are shown in Fig. 5(a)−Fig. 5(c). On the whole, the outputs of these three algorithms are all defocused, due to the mismatch among the beginning/ending time of the target signal and RFRFT, GRFT as well as the RFT. Compared to the integration results of GRFT and RFT (which are seriously defocused) the integration result of RFRFT seems slightly better, but there is still no obvious peak in Fig. 5(a). More importantly, the relatively high peak position of Fig. 5(a) does not appear at the position corresponding to the target's motion parameters, which means that the target's motion parameters cannot be accurately estimated.
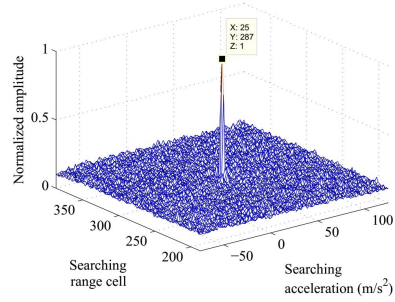
4.2. Parameters Estimation Performance

The estimation performances (i.e., root-mean-squared error (RMSE)) of the proposed WRFRFT algorithm for target's motion parameters (range, ve-
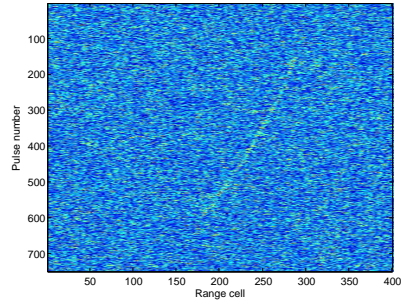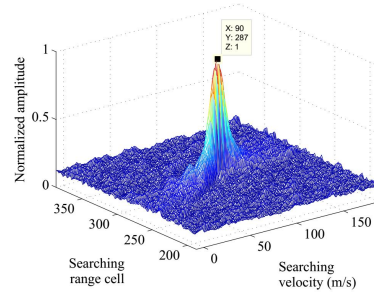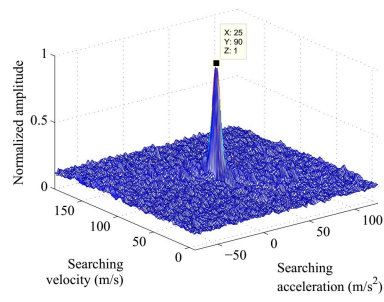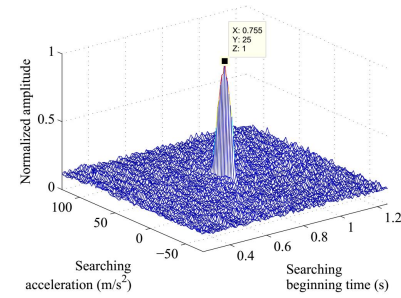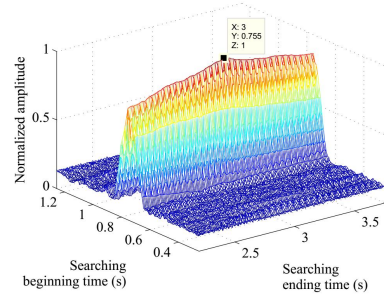
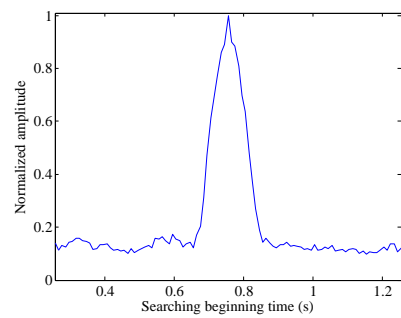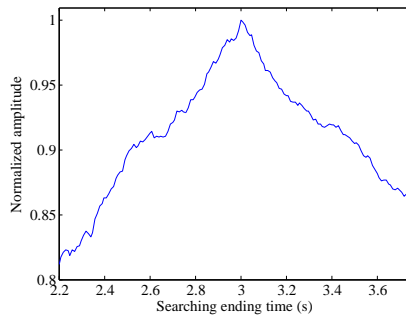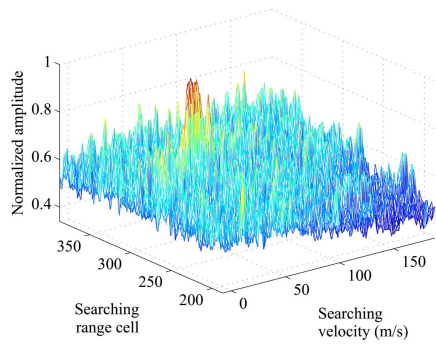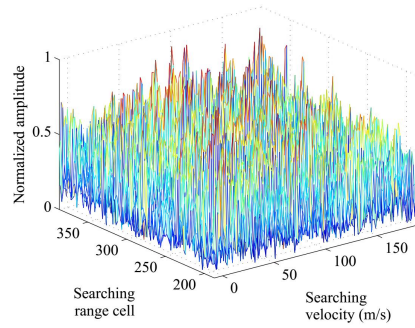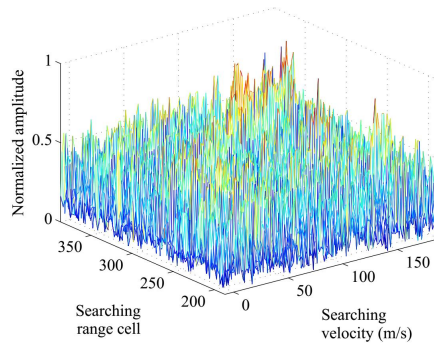Figure 4: WRFRFT for a weak target. (a) PC. (b) Projection in range cell-velocity domain. (c) Projection in range cell-acceleration domain. (d) Projection in velocity-acceleration domain. (e) Projection in acceleration-beginning time domain. (f) Projection in beginning time-ending time domain. (g) Beginning time response slice. (h) Ending time response slice.

Figure 5: Integration results of (a) RFRFT. (b) GRFT. (c) RFT.

locity and acceleration) and time parameters (beginning/ending time) under different SNR levels are evaluated by Monte Carlo experiment. Fig. 6 gives the estimation performance curves of target's motion parameters, where 200 times Monte Carlo trails are performed for each SNR. From Fig. 6, we can notice that the WRFRFT has a better estimation ability than RFRFT and it could obtain good estimation performance when the SNR is larger than -10 dB. Additionally, Fig. 7 shows the RMSE curves of target's time parameters where similar behaviors are observed.
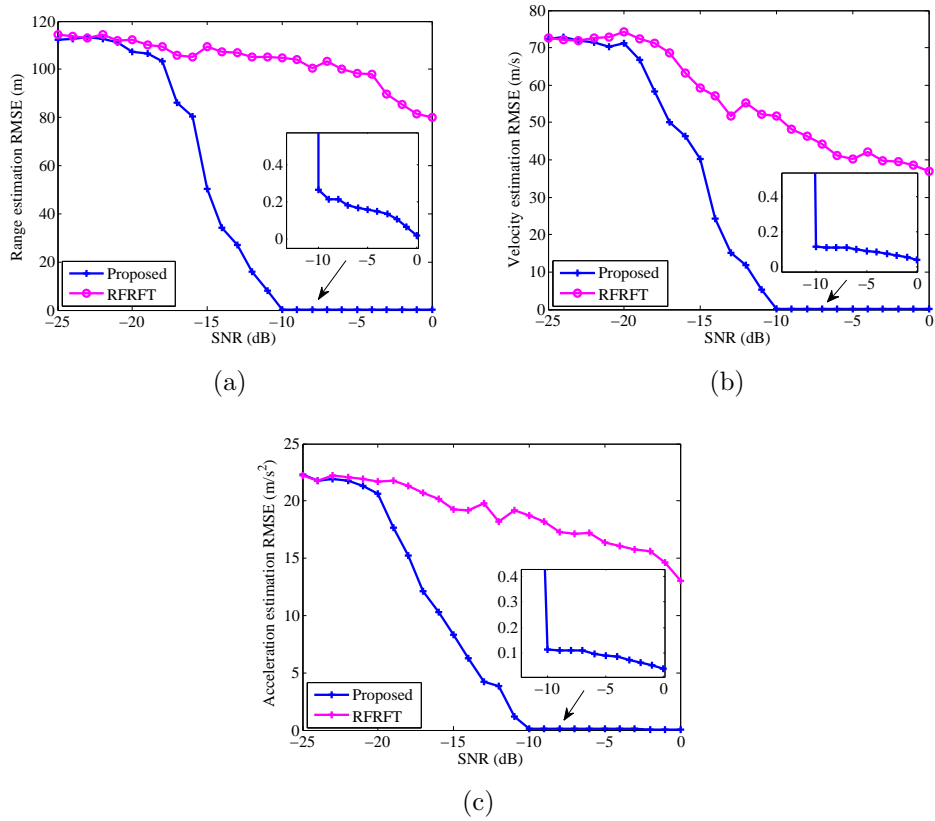

(a)   (b)

(c)

Figure 6: RMSE of the estimated motion parameters. (a) Range. (b) Velocity. (c) Acceleration.

4.3. Detection Ability

The detection performances of the WRFRFT method, RFRFT, GRFT, MTD and RFT under different SNR are shown in Fig. 8, where the false
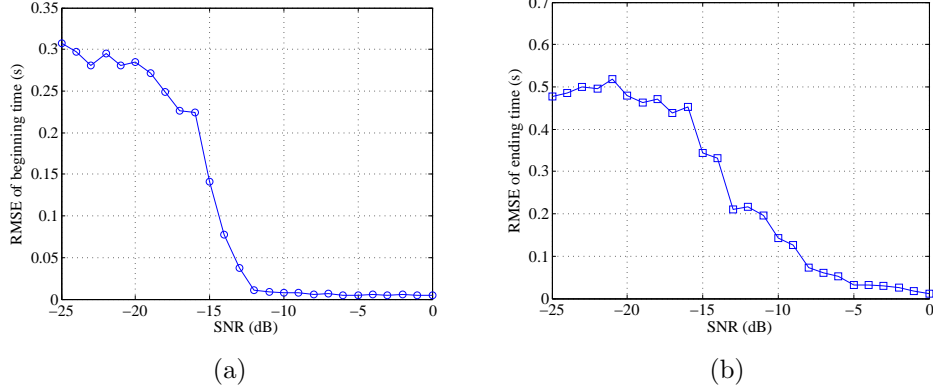
Figure 7: RMSE of the estimated time parameters. (a) Beginning time (entry). (b) Ending time (departure).

alarm rate is set as $P_f = 10^{-5}$. From Fig. 8, it could be noticed that the proposed WRFRFT method could obtain better detection probability than RFRFT, GRFT and RFT thanks to its ability of matching with the target's beginning time and ending time as well as the correction of ARC and DS. For example, WRFRFT is able to detect a target with 0.8 probability at SNR 10/11.5/15.6 dB lower than RFRFT/GRFT/RFT respectively.

4.4. WRFRFT for Multiple Targets

Fig. 9 shows the simulation results of WRFRFT for multiple targets. Four moving targets (denoted as T_1, T_2, T_3 and T_4) are considered and the parameters are listed in Table 3. The target motion trajectories after range compression are shown in Fig. 9(a), where the four curved trajectories are observed. Fig. 9(b)−Fig. 9(d) give respectively different slices of WRFRFT output.

More specifically, Fig. 9(b) shows the WRFRFT result with $a_s = 25\mathrm{m/s}^2$, $\eta_{0s} = 0.755$s, $\eta_{1s} = 3$s. Note that the searching values of acceleration, beginning/ending time are match with the corresponding parameters of T_1 and T_2. Hence, the signal energy of T_1 and T_2 are coherently accumulated and the targets are are well focused as seen from the two peaks in this slice (Fig. 9(b)). However, because of the searching values of acceleration, beginning time and ending time in this slice are not matched with T_3 and T_4 and thus the signal energy of T_3 and T_4 can not be coherently integrated in this slice.

Fig. 9(c) shows the WRFRFT result with $a_s = 17\mathrm{m/s}^2$, $\eta_{0s} = 0.905$s,
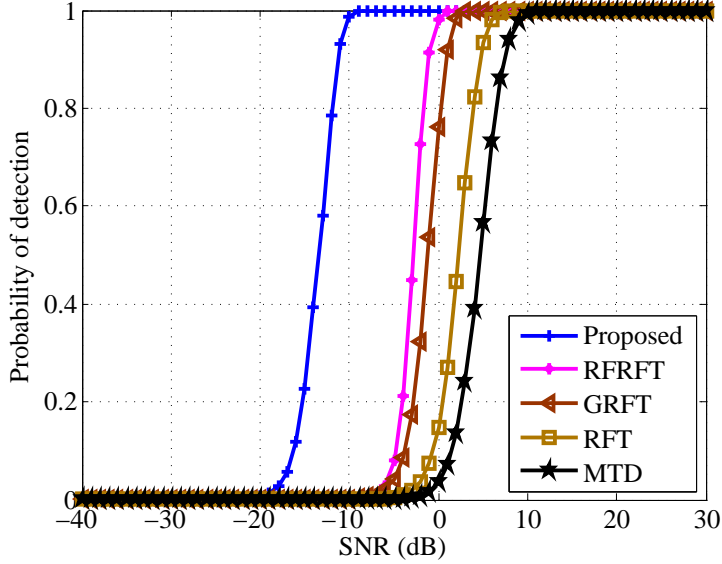
Figure 8: Detection ability curves.

$\eta_{1s} = 3.4$s, which is matched with the acceleration and beginning/ending time of T_3. Correspondingly, the target signal of T_3 is coherently focused as a peak in this slice (Fig. 9(c)). Moreover, Fig. 9(d) shows the WRFRFT result with $a_s = 13$m/s^2, $\eta_{0s} = 1.005$s, $\eta_{1s} = 3.2$s. In this slice (Fig. 9(d)), the searching values of acceleration and beginning/ending time match with the parameters of T_4 and thus we could notice that there is a peak formed, which is corresponding to T_4.

4.5. Real Data Results

To verify the effectiveness of the WRFRFT method, an evaluation is made using real collected data. The data set is the target signal of an unmanned aerial vehicle (UAV). Its maximum speed is 60 m/s and its maximum acceleration is 10 m/s^2. The detection system was a LFM pulse radar, the detailed parameters are listed in Table 4. During the experiment, the target did not appear in the radar detection beam for the early stage of radar startup, so there was only noise and clutter, but no target echo signal. Then, the UAV flew into the radar detection area, and the radar received the echo signal of the UAV. The UAV flew out of the radar detection area a few seconds later,
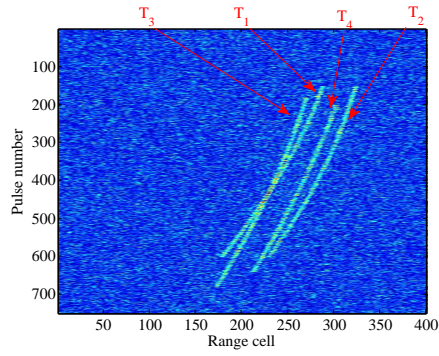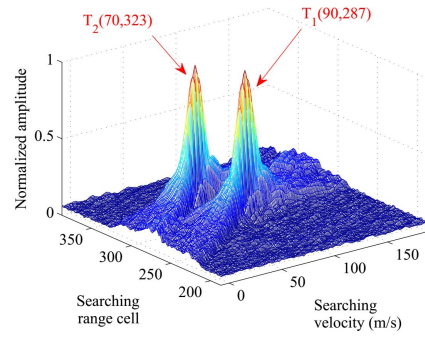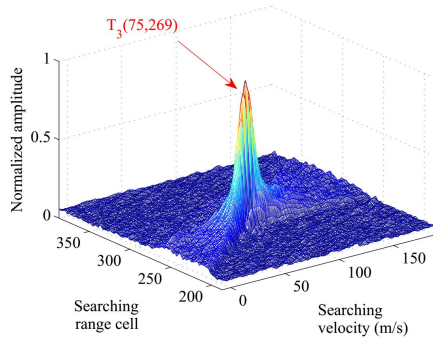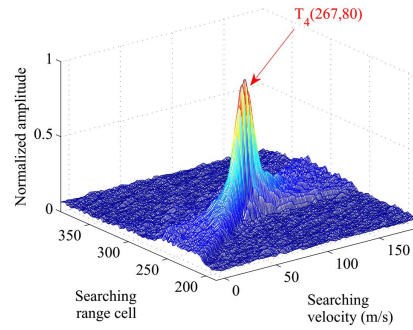
Figure 9: Multiple targets scene. (a) Results after pulse compression. (b) The focusing result of T_1 and T_2 with $a_s = 25\text{m/s}^2, \eta_{0s} = 0.755\text{s}, \eta_{1s} = 3\text{s}$. (c) The focusing result of T_3 with $a_s = 17\text{m/s}^2, \eta_{0s} = 0.905\text{s}, \eta_{1s} = 3.4\text{s}$. (d) The focusing result of T_4 with $a_s = 13\text{m/s}^2, \eta_{0s} = 1.005\text{s}, \eta_{1s} = 3.2\text{s}$.
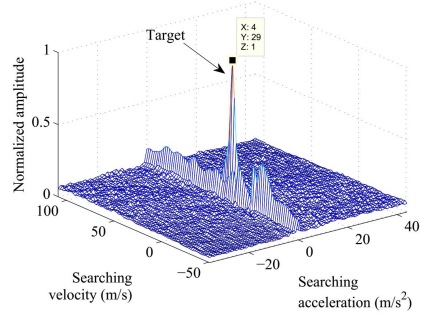
Table 3

Parameters of the Four Moving Targets

Parameter	T_1	T_2	T_3	T_4
Initial range cell	287	323	269	305
Velocity (m/s)	90	70	75	95
Acceleration m/s^2	25	25	17	13
Beginning time (s)	0.705	0.705	0.905	1.005
Ending time (s)	3	3	3.4	3.2
SNR after PC	6dB	6dB	6dB	6dB

but the radar was still transmitting and receiving signals after the UAV's departure.

The selected data to be processed consists of 2000 pulses (i.e., coherent processing interval is 4 s), as show in Fig. 10(a), from which we could see that the target motion trajectory crosses several range cells. In particular, we could choose "two points" (as shown in Fig. 10(a)) from the target's moving trajectory to obtain a rough estimation of target's velocity, i.e., $v = (79 - 72) \times 2.5\text{m}/(1.428s - 0.974s) = 27.533\text{m}/s$. After WRFRFT, the focusing result of target is given in Fig. 10(b). We could notice that the target signal is focused as a peak and its position represents the target's velocity and acceleration (i.e., $29\text{m}/s$ and $4\text{m}/s^2$). For comparison, the processing results of RFRFT and GRFT are also given in Fig. 10(c) and Fig. 10(d), respectively. For the focusing result of RFRFT (Fig. 10(c)), it could be noticed that there is no significant peak in the RFRFT output and noted that the "pseudo or false peak" location is corresponding to $-9\text{m}/s$ and $0\text{m}/s^2$. In addition, the "pseudo or false peak" location of GRFT (Fig. 10(d)) is corresponding to $-25\text{m}/s$ and $0\text{m}/s^2$. Therefore, both RFRFT and GRFT could not focus the target signal correctly, resulting in estimation error and even false alarm. Furthermore, the beginning-time response slice and ending-time response slice of WRFRFT are given in Fig. 10(e) and Fig. 10(f), respectively. From Fig. 10(e) and Fig. 10(f), we could obtain the estimations of target signal's beginning/ending time, i.e., 0.602 s and 3.406 s.
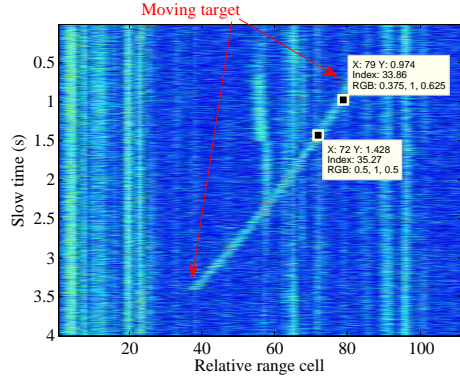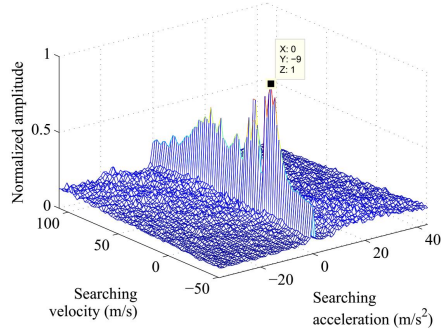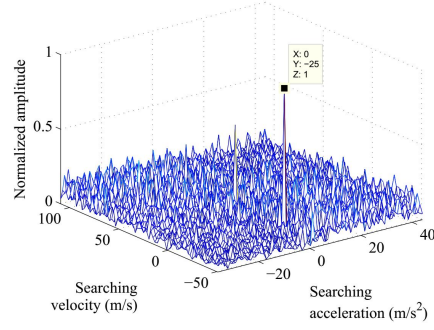
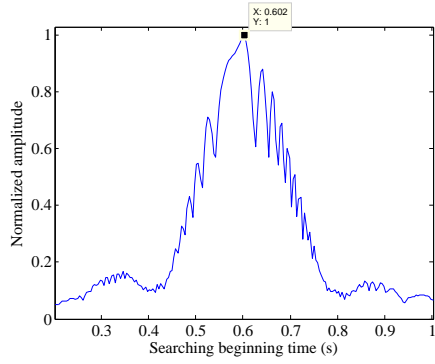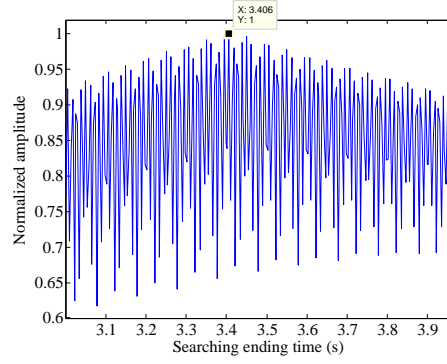Figure 10: Real data results. (a) Compressed echoes. (b) The focusing result of WRFRFT. (c) Integration result of RFRFT. (d) Integration result of GRFT. (e) Beginning time response slice. (f) Ending time response slice.

25

Table 4

Radar Parameters for Real Data

Wave band	C
Bandwidth	20 MHz
Sample frequency	60 MHz
Pulse repetition frequency	500 Hz
Pulse duration	18 us

5. Conclusion

In this paper, a new coherently focusing and parameters estimation method (i.e., WRFRFT) has been proposed for a radar maneuvering target with ARC and DS effects, where the times of the target appears in and leaves the radar detection area are unknown. By employing the window function and searching along the target moving trajectory, the echo signal of a maneuvering target could be well matched and focused as a peak in the WRFRFT domain and the target's time parameters (entry time and departure time) and motion parameters (range, velocity and acceleration) could be estimated via the peak location. The performances are validated by detailed experiments using simulated data and real data.

References

[1] W. C. Yu, W. M. Su, and H. Gu, "Ground maneuvering target detection based on discrete polynomial-phase transform and Lv's distribution," *Signal Processing*, vol. 144, pp. 364–372, March 2018.

[2] X. L. Li, G. L. Cui, W. Yi, and L. J. Kong, "Radar maneuvering target detection and motion parameter estimation based on TRT-SGRFT," *Signal Processing*, vol. 133, pp. 107–116, April 2017.

[3] C. Sun, B. P. Wang, Y. Fang, K. F. Yang, and Z. X. Song, "High-resolution ISAR imaging of maneuvering targets based on sparse reconstruction," *Signal Processing*, vol. 108, pp. 535–548, March 2015.

[4] H. Zhong, and X. Z. Liu, "An effective focusing approach for azimuth invariant bistatic SAR processing," *Signal Processing*, vol. 90, no.1, pp. 395–404, January 2010.

[5] J. B. Zheng, T. Su, H. W. Liu, G. S. Liao, Z. Liu, and Q. H. Liu, "Radar high-speed target detection based on the frequency-domain deramp-keystone transform," *IEEE J. Sel. Topics Appl. Earth Obs. Remote Sens.*, vol. 9, no.1, pp. 285–294, January 2016.

[6] P. H. Huang, X. Xia, G. S. Liao, and Z. W. Yang, "Ground moving target imaging based on keystone transform and coherently integrated CPF with a single-channel SAR," *IEEE J. Sel. Topics Appl. Earth Obs. Remote Sens.*, vol. 10, no.12, pp. 5686–5694, December 2017.

[7] J. C. Zhang, T. Su, J. B. Zheng, and X. H. He, "Novel fast coherent detection algorithm for radar maneuvering target with jerk motion," *IEEE J. Sel. Topics Appl. Earth Obs. Remote Sens.*, vol. 10, no.5, pp. 1792–1803, May 2017.

[8] J. B. Zheng, H. W. Liu, G. S. Liu, T. Su, Z. Liu and Q. H. Liu, "ISAR imaging of nonuniformly rotating targets based on generalized decoupling technique ," *IEEE J. Sel. Topics Appl. Earth Obs. Remote Sens.*, vol. 9, no.1, pp. 520–532, January 2016.

[9] X. L. Li, Z. Sun, W. Yi, G. L. Cui, and L. J. Kong, "Radar detection and parameter estimation of high speed target based on MART-LVT," *IEEE Sensors Journal.*, vol. 19, no. 4, pp. 1478–1486, February 2019.

[10] X. L. Chen, Y. Huang, N. B. Liu, J. Guan, and Y. He, "Radon-fractional ambiguity function-based detection method of low-observable maneuvering target," *IEEE Trans. Aerosp. Electron. Syst.*, vol. 51, no. 2, pp. 815–833, April 2015.

[11] S. Q. Zhu, G. S. Liao, D. Yang, and H. H. Tao, "A new method for radar high-speed maneuvering weak target detection and imaging," *IEEE Geoscience and Remote Sensing Letters*, vol. 11, no. 7, pp. 1175–1179, July 2014.

[12] J. Tian, W. Cui, and S. Wu, "A novel method for parameter estimation of space moving targets," *IEEE Geoscience and Remote Sensing Letters*, vol. 11, no. 2, pp. 389–393, February 2014.

[13] X. L. Chen, J. Guan, Y. Huang, N. B. Liu, and Y. He, "Radon-linear canonical ambiguity function-based detection and estimation method for

marine target with micromotion," *IEEE Trans. Geosci. Remote Sens.*, vol. 53, no. 4, pp. 2225–2240, April 2015.

[14] P. H. Huang, G. S. Liao, Z. W. Yang, X. G. Xia, J. T. Ma, and J. B. Zheng, "Ground maneuvering target imaging and high-order motion parameter estimation based on second-order keystone and generalized Hough-HAF transform," *IEEE Trans. Geosci. Remote Sens.*, vol. 55, no. 1, pp. 320–335, January 2017.

[15] J. Xu, Y. N. Peng, X. G. Xia, T. Long, E. K. Mao, and A. Farina, "Focus-before-detection radar signal processing: part ii-recent developments," *IEEE Aerosp. Electron. Syst. Magazine*, vol. 33, no. 1, pp. 34–49, January 2018.

[16] P. H. Huang, G. S. Liao, Z. W. Yang, X. Xia, J. T. Ma, and J. T. Ma, "Long-time coherent integration for weak maneuvering target detection and high-order motion parameter estimation based on keystone transform," *IEEE Trans. Signal Process.*, vol. 64, no. 15, pp. 4013–4026, August 2016.

[17] X. L. Li, G. L. Cui, W. Yi, and L. J. Kong, "Fast coherent integration for maneuvering target with high-order range migration via TRT-SKT-LVD," *IEEE Trans. Aerosp. Electron. Syst.*, vol. 52, no. 6, pp. 2803–2814, December 2016.

[18] Z. Sun, X. L. Li, W. Yi, G. L. Cui, and L. J. Kong, "A coherent detection and velocity estimation algorithm for the high-speed target based on the modified location rotation transform," *IEEE J. Sel. Topics Appl. Earth Obs. Remote Sens.*, vol .11, no. 7, pp. 2346-2361, July 2018.

[19] X. L. Li, G. L. Cui, W. Yi, and L. J. Kong, "Sequence-reversing transform-based coherent integration for high-speed target detection," *IEEE Trans. Aerosp. Electron. Syst.*, vol. 53, no. 3, pp. 1573–1580, June 2017.

[20] J. Xu, J. Yu, Y. N. Peng, and X. G. Xia, "Radon-fourier transform (RFT) for radar target detection (I): generalized doppler filter bank processing," *IEEE Trans. Aerosp. Electron. Syst.*, vol. 47, no. 2, pp. 1186–1202, April 2011.

[21] J. Xu, J. Yu, Y. N. Peng, and X. G. Xia, "Radon-fourier transform (RFT) for radar target detection (II): blind speed sidelobe suppression," *IEEE Trans. Aerosp. Electron. Syst.*, vol. 47, no. 4, pp. 2473–2489, October 2011.

[22] J. Yu, J. Xu, Y. N. Peng, and X. G. Xia, "Radon-fourier transform (RFT) for radar target detection (III): optimality and fast implementations," *IEEE Trans. Aerosp. Electron. Syst.*, vol. 48, no. 2, pp. 991–1004, April 2012.

[23] J. B. Zheng, T. Su, W. T. Zhu, X. H. He, and Q. H. Liu, "Radar high-speed target detection based on the scaled inverse Fourier transform," *IEEE J. Sel. Topics Appl. Earth Obs. Remote Sens.*, vol. 8, no.3, pp. 1108–1119, March 2015.

[24] R. P. Perry, R. C. Dipietro, and R. L. Fante, "SAR imaging of moving targets," *IEEE Trans. Aerosp. Electron. Syst.*, vol. 35, no. 1, pp. 188–200, January 1999.

[25] G. Li, X. G. Xia, and Y. N. Peng, "Doppler keystone transform: An approach suitable for parallel implementation of SAR moving target imaging," *IEEE Geoscience and Remote Sensing Letters*, vol. 5, no. 4, pp. 573–577, October 2008.

[26] D. Y. Zhu, Y. Li, and Z. D. Zhu, "A keystone transform without interpolation for SAR ground moving-target imaging," *IEEE Geoscience and Remote Sensing Letters*, vol. 4, no. 1, pp. 18–22, Janunary 2007.

[27] J. Xu, X. G. Xia, S. B. Peng, J. Yu, Y. N. Peng, and L. C. Qian, "Radar maneuvering target motion estimation based on generalized radon-fourier transform," *IEEE Trans. Signal Process.*, vol. 60, no. 12, pp. 6190–6201, December 2012.

[28] X. L. Li, G. L. Cui, W. Yi, and L. J. Kong, "Coherent integration for maneuvering target detection based on Radon-Lv's distribution," *IEEE Signal Processing Letters*, vol. 22, no. 9, pp. 1467–1471, September 2015

[29] X. L. Chen, J. Guan, N. B. Liu, and Y. He, "Maneuvering target detection via Radon-Fractional Fourier transform-based long-time coherent integration," *IEEE Trans. Signal Process.*, vol. 62, no. 4, pp. 939–953, February 2014.

[30] X. L. Li, Z. Sun, T. S. Yeo, T. X. Zhang, W. Yi, G. L. Cui, and L. J. Kong, "STGRFT for detection of maneuvering weak target with multiple motion models," *IEEE Trans. Signal Process.*, vol. 67, no. 7, pp. 1902–1917, April 2019.

[31] X. L. Li, Z. Sun, W. Yi, G. L. Gui, L. J. Kong, and X. B. Yang "Computationally efficient coherent detection and parameter estimation algorithm for maneuvering target," *Signal Processing*, vol. 155, pp. 130–142, February 2019.

[32] X. L. Li, G. L. Cui, W. Yi, and L. J. Kong, "A fast maneuvering target motion parameters estimation algorithm based on ACCF," *IEEE Signal Processing Letters*, vol. 22, no. 3, pp. 270–274, March 2015.

[33] X. L. Li, G. L. Cui, L. J. Kong, and W. Yi, "Fast non-searching method for maneuvering target detection and motion parameters estimation," *IEEE Trans. Signal Process.*, vol. 64, no. 9, pp. 2232–2244, May 2016.

[34] X. L. Li, L. J. Kong, G. L. Cui, and W. Yi, "A fast detection method for maneuvering target in coherent radar," *IEEE Sensors Journal*, vol. 15, no. 11, pp. 6722–6729, November 2015.

[35] Z. Sun, X. L. Li, W. Yi, G. L. Gui, and L. J. Kong, "Detection of weak maneuvering target based on keystone transform and matched filtering process," *Signal Processing*, vol. 140, pp. 127–138, November 2017.

[36] J. B. Zheng, H. W. Liu, J. Liu, X. L. Du, and Q. H. Liu, "Radar high-speed maneuvering target detection based on three-dimensional scaled transform," *IEEE J. Sel. Topics Appl. Earth Obs. Remote Sens.*, vol. 11, no.8, pp. 2821–2833, August 2018.